

EarthArXiv

**Seasonal Shift in the Dominant Pathway Energizing Mesoscale
Eddies in the California Current**

Authors

Jack F. Gazeley¹
Sarah T. Gille¹
Lia Siegelman¹
Alberto C. Naveira Garabato²
Jackie May³
Joseph D'Addezio³
Shang-Ping Xie¹

¹ Scripps Institution of Oceanography, University of California, San Diego, USA

² Ocean and Earth Science, National Oceanography Centre, University of Southampton, UK

³ U.S. Naval Research Laboratory, Ocean Sciences Division, Stennis Space Center, USA

Corresponding author: Jack F. Gazeley
Email: jgazeley@ucsd.edu

Preprint Statement

This manuscript is a non-peer-reviewed preprint submitted to EarthArXiv.

This manuscript has been submitted to the *Journal of Physical Oceanography* for peer review.

Copyright in this work may be transferred without further notice.

1 **Seasonal Shift in the Dominant Pathway Energizing Mesoscale Eddies in the**
2 **California Current**

3 Jack F. Gazeley^a, Sarah T. Gille^a, Lia Siegelman^a, Alberto C. Naveira Garabato^b, Jackie May^c,
4 Joseph D'Addezio^c, Shang-Ping Xie^a

5 ^a *Scripps Institution of Oceanography, University of California, San Diego, California, US*

6 ^b *Ocean and Earth Science, National Oceanography Centre, University of Southampton,*
7 *Southampton, UK*

8 ^c *U.S Naval Research Laboratory, Ocean Sciences Division, Stennis Space Center, Mississippi, US*

9 *Corresponding author: Jack F. Gazeley, jgazeley@ucsd.edu*

10 ABSTRACT: Mesoscale eddies are the dominant reservoir of kinetic energy in the ocean, yet
11 the mechanisms that generate and maintain them in eastern boundary current systems remain
12 incompletely assessed. Here we use a 1-km resolution simulation of the California Current
13 System (CCS) to diagnose and quantify the processes that supply kinetic energy to the mesoscale
14 band. A pronounced seasonal transition is evident in surface vorticity, kinetic energy spectra, and
15 mixed-layer depth. In winter and spring, the mixed layer deepens during periods of strong wind
16 work. Once the forcing relaxes, the mixed layer restratifies, generating submesoscale eddies and
17 filaments. These features merge and transfer energy upscale, supplying the mesoscale through an
18 inverse cascade. These mixed-layer restratification events occur most frequently when the mixed
19 layer is deep (~50 m) and highly variable. In contrast, during summer when the mixed layer
20 is shallow, a mixed-layer-averaged geostrophic kinetic energy budget indicates that wind work
21 accelerates the surface layer of the ocean more efficiently. This is associated with enhanced kinetic
22 energy transfer from scales larger than 100 km into the mesoscale. Together, these results indicate a
23 seasonally varying balance between inverse and direct kinetic energy transfers in the CCS, implying
24 that the annual cycle of upper-ocean stratification leads to a seasonal shift in the dominant pathway
25 of mesoscale eddy generation.

26 SIGNIFICANCE STATEMENT: Upper-ocean stratification influences ocean surface currents
27 through multiple mechanisms, but the relative importance of these mechanisms has not been
28 quantified. Stronger stratification can trap wind forcing in a shallow layer and accelerate surface
29 currents, while weaker stratification increases available potential energy variance and promotes
30 submesoscale instabilities. In this study, we show that both mechanisms are important in the
31 dynamics of the California Current System but dominate at different times of year and at different
32 scales. In summer, shallow mixed layers favor accelerated surface currents and a forward cascade
33 from larger scales. In winter and spring, mixed-layer instabilities energize the mesoscale through
34 an inverse cascade. Additionally, the importance of the inverse cascade implies that unresolved
35 submesoscale motions can influence mesoscale variability and therefore have consequences for
36 ocean predictability.

37 **1. Introduction**

38 The mesoscale eddy field, with horizontal scales of $O(100)$ km, accounts for up to 80% of the
39 kinetic energy in the global ocean (Ferrari and Wunsch 2009). Mesoscale eddies play a central
40 role in transporting tracers and regulating marine ecosystems by modulating nutrient supply and
41 biological productivity (McGillicuddy et al. 2007). They dominate lateral stirring and set the
42 effective diffusivity of tracers in the ocean (Ferrari and Nikurashin 2010). The mesoscale circulation
43 also governs the structure of wave–eddy interactions, controlling the transmission of internal wave
44 energy into the ocean interior and its subsequent contribution to diapycnal mixing (Asselin and
45 Young 2020). The oceanic mesoscale is an essential component of air–sea interactions, biophysical
46 coupling, and the global kinetic energy budget. Yet, despite the oceanic mesoscale’s importance,
47 the relative contributions of the processes that generate and maintain mesoscale energy have not
48 been fully reconciled across different circulation regimes, particularly on seasonal-to-interannual
49 timescales.

50 The prevailing paradigm is that oceanic mesoscale kinetic energy is generated and maintained
51 through a combination of large-scale forcing and cross-scale kinetic energy cascades, rather than by
52 direct forcing at mesoscale wavelengths alone. At leading order, mesoscale eddies are traditionally
53 understood to draw energy from the large-scale circulation through baroclinic instability, converting
54 available potential energy associated with mean buoyancy gradients into eddy kinetic energy at

55 scales of order of the first baroclinic Rossby radius (Vallis 2017; Ferrari and Wunsch 2009). This
56 injection feeds a predominantly downscale direct cascade of kinetic energy toward smaller scales
57 and ultimately dissipation, consistent with classical views of geostrophic turbulence (Charney
58 1971; Vallis 2017). In this framework, energy is input into the ocean primarily by wind forcing
59 at large spatial scales, typically exceeding 250 km (Rai et al. 2021). Recent work further suggests
60 that the efficiency of this large-scale wind-driven momentum input may depend on upper-ocean
61 stratification, with surface currents more readily accelerating when mixed layers are shallow, since
62 the same wind stress can be more efficiently transferred into a layer with less inertia (Peng et al.
63 2022). Such modulation of the large-scale flow has the potential to influence the amount of kinetic
64 energy available for mesoscale baroclinic instability and the direct cascade, thereby affecting the
65 energization of the mesoscale. However, a quantitative assessment of the relative importance of
66 this pathway in setting mesoscale energetics has yet to be established.

67 In contrast, high-resolution numerical simulations and observations have demonstrated that
68 significant energy can also be injected at submesoscales through mixed-layer instabilities (MLIs).
69 Episodes of rapid mixed-layer deepening followed by restratification are frequently accompanied by
70 an injection of submesoscale kinetic energy (Boccaletti et al. 2007; Sasaki et al. 2014; Fox-Kemper
71 et al. 2008) that can transfer upscale through an inverse cascade and merge into the mesoscale band
72 (Capet et al. 2008a; Schubert et al. 2020; Sasaki et al. 2014). The seasonality of the submesoscale
73 structures is strongly modulated by the seasonal cycle in mixed-layer depth (MLD) via MLIs
74 (Brannigan et al. 2015; Callies et al. 2015; Rocha et al. 2016; Sasaki et al. 2014; Qiu et al.
75 2014). During winter and early spring, surface cooling and enhanced wind forcing deepen the
76 mixed layer and weaken stratification, allowing strong lateral buoyancy gradients to persist within
77 the mixed layer (Holte et al. 2017; Zhang et al. 2018). These conditions are conducive to the
78 growth of MLIs, which act to restratify the mixed layer and smooth horizontal buoyancy gradients
79 through ageostrophic motions (Boccaletti et al. 2007; Fox-Kemper et al. 2008). Some studies have
80 hypothesized that the pronounced seasonal variability of submesoscale activity may also contribute
81 to the seasonal cycle of mesoscale kinetic energy through an inverse kinetic energy cascade (Sasaki
82 et al. 2014; Qiu et al. 2014; Naveira-Garabato et al. 2022; Khatri et al. 2021). In contrast, other
83 work has emphasized that submesoscale variability exhibits a strong seasonal cycle even in regions
84 where mesoscale energy shows comparatively weak seasonality (Callies et al. 2015; Buckingham

85 et al. 2016). However, a systematic quantification of the cumulative contribution of MLI-driven
86 inverse transfers to the mesoscale energy budget, and a direct comparison of this pathway with the
87 classical mesoscale baroclinic instability of the large-scale flow, has not yet been established. In
88 particular, the relative importance of these two pathways under different stratification and forcing
89 regimes remains an open area of research.

90 In this study, we quantify the relative contributions of these energetic pathways to mesoscale
91 kinetic energy in the California Current System (CCS). The CCS is an eastern boundary current
92 characterized by strong seasonal variability in surface forcing and stratification. The CCS undergoes
93 a pronounced seasonal cycle associated with storm activity and upwelling, which drives large
94 variations in mixed-layer depth, surface buoyancy fluxes, and alongshore wind stress (Di Lorenzo
95 2003). These seasonal changes are accompanied by substantial reorganization of the surface
96 circulation. In winter and early spring, persistent upwelling-favorable winds maintain sloped
97 coastal isopycnals that support a strong equatorward jet, while the coastal poleward return flow
98 is absent. As upwelling relaxes in summer, positive wind-stress curl over the continental slope
99 drives the development of a pronounced poleward return flow, a transition well documented in
100 climatological observations (Di Lorenzo 2003). This adjustment is associated with a flattening
101 of coastal isopycnals and the offshore propagation of mesoscale features in the form of westward-
102 propagating Rossby waves generated by baroclinic instability of the mean flow. High-resolution
103 numerical simulations have demonstrated that the CCS supports energetic variability across a
104 wide range of scales, including both mesoscale eddies and vigorous submesoscale motions (Torres
105 et al. 2024; Farrar et al. 2025), with their relative prominence varying seasonally (Capet et al.
106 2008a,b). A quantitative assessment of how seasonally varying stratification modulates the relative
107 contributions of large-scale and submesoscale pathways to mesoscale energetics is lacking.

108 Despite substantial progress on both mixed-layer instability dynamics and mean-flow baroclinic
109 instability in boundary current systems, a clear gap remains in quantifying how these pathways
110 jointly contribute to the mesoscale kinetic energy in the CCS, and how their relative importance
111 varies seasonally. In this study, we address this problem using a 1-km resolution simulation of the
112 CCS from March–October 2023. We first characterize the seasonal evolution of the ocean dynamics
113 and their energetics in the CCS in Section 3a. We then examine the mechanisms driving MLIs
114 and their associated submesoscale energy injection using a composite of more than 300 events in

115 Section 3b. In Section 3c, we demonstrate that large-scale forcing of the circulation is dominated
116 by wind-driven momentum trapping during the shallow mixed layer season, by considering a
117 geostrophic mixed-layer averaged budget. Finally, in Section 3d, we compare and quantify the
118 relative importance of these two mechanistic pathways in supplying kinetic energy via inverse and
119 direct kinetic energy cascades to the mesoscale band over the annual cycle, using a coarse-grained
120 cross-scale kinetic energy transfer diagnostic framework. Section 4 discusses the implications of
121 the work after summarizing and contextualizing within the existing literature.

122 **2. Data and Methods**

123 *a. Data*

124 The Coupled Ocean Atmosphere Modelling Prediction System (COAMPS, Allard et al. 2015)
125 version 2021.1 is used in this study. COAMPS includes modelling components representing the
126 ocean, atmosphere, waves, and ice and has the ability to run these components in a stand-alone or
127 coupled configuration. For this study, only the ocean component, the Navy Coastal Ocean Model
128 (NCOM, Barron et al. 2006), is run as a stand-alone system over the CCS region. The modelled
129 domain extends from 230° – 244.5° W and 30° – 42° N with a 1-km horizontal resolution. There
130 are 100 vertical levels with 36 terrain following sigma layers on top of 64 constant depth levels
131 (z -levels), with the transition between the sigma and z -levels occurring at 150 m. The surface
132 sigma layer is 1.5 m thick with continuous stretching applied to subsequent layers, extending to a
133 maximum ocean bottom depth of 5500 m.

134 NCOM is a primitive equation model that uses the hydrostatic and Boussinesq approximations.
135 In this study, NCOM utilizes the Mellor and Yamada (1982) level-2 vertical mixing scheme and the
136 Smagorinsky (1963) horizontal diffusion scheme. Horizontal boundary conditions were obtained
137 from 3 h output from the $1/12^{\circ}$ horizontal resolution Global Ocean Forecasting System (GOFS,
138 Metzger et al. 2015) version 3.5. Atmospheric forcing fields were provided with a frequency of 3 h
139 by the 0.5° horizontal resolution global atmospheric model, NAVy Global Environmental Model
140 (NAVEM, Hogan et al. 2015). Fresh water river in flow fluxes were estimated from the NCOM
141 monthly climatology river data base (Barron and Smedstad 2002). NCOM barotropic tidal forcing
142 was applied using the global Oregon Tidal Inverse Solution (OTIS, Egbert and Erofeeva 2002).
143 Barotropic tidal interactions with bathymetry introduce baroclinic tides into the simulation.

144 Ocean data assimilation is performed daily at 00z with the Navy Coupled Ocean Data Assimila-
 145 tion (NCODA) three-dimensional variational (3DVAR) analysis system (Daley and Barker 2001;
 146 Cummings et al. 2010; Cummings 2005). Observations that are assimilated include temperature,
 147 salinity, and sea surface height anomalies (SSHA). Temperature and salinity profiles are obtained
 148 from in situ platforms; SSHA observations are obtained from the nadir altimeters onboard the Joint
 149 Altimetry Satellite Oceanography Network (JASON)-3, Sentinel-3A, Sentinel-3B, and Satellite
 150 with ARgos and ALtika (SARAL) platforms; and sea surface temperature (SST) observations are
 151 obtained from ships, buoys, floats and satellite sensors onboard the Meteorological operational
 152 satellite (Metop)-C, National Oceanic and Atmospheric Administration (NOAA)-20, and Suomi
 153 National Polar-orbiting Partnership (S-NPP) platforms. The data assimilation window is set to 48 h
 154 for in situ profiles, 120 h for nadir altimeters, and 24 h for SST. This single-scale configuration of
 155 NCODA-3DVAR is expected to only correct for large, mesoscale ocean features, leaving smaller
 156 submesoscales mostly unaltered during the update cycle (D’Addezio et al. 2019).

157 *b. Mixed-Layer Depth*

158 The mixed-layer depth (MLD) is used in this study to characterize the seasonal cycle in stratifi-
 159 cation and forcing, define and detect deepening–restratification events that energize submesoscale
 160 motions (Section 3b), and interpret the seasonal transition in mesoscale forcing and eddy scale
 161 (Section 3d). Here we define the MLD following Reichl et al. (2022), as the depth of uppermost
 162 layer that reaches a pre-defined potential energy (PE) anomaly. The PE anomaly of a seawater layer
 163 quantifies the wind work required to homogenize its density. The MLD is defined as the depth at
 164 which the simplified PE anomaly of the layer equals a prescribed value, ϕ :

$$\phi = \int_{-h}^{\eta} (\rho_m - \rho_i) g z \, dz, \quad (1)$$

165 where

$$\rho_m = \frac{1}{\eta + h} \int_{-h}^{\eta} \rho_i \, dz, \quad (2)$$

166 is the density the layer would have if fully mixed, i.e., the mean density within the layer. Equation 1
 167 can be inverted for h for a given ϕ using a Newton–Raphson algorithm (Reichl et al. 2022).
 168 However, it is often computationally cheaper to compute the simplified PE anomaly for all possible

169 values of h and interpolate to the target value of ϕ . The PE anomaly method requires specifying
 170 a value of ϕ , which was empirically tuned using wind-work diagnostics following Reichl et al.
 171 (2022).

172 *c. Wavenumber–Frequency Spectrum*

173 Wavenumber and wavenumber–frequency spectra are used in Section 3a to quantify how the
 174 energetic distribution across scales and frequencies changes between winter/spring and summer.
 175 The isotropic wavenumber–frequency ($\omega - k$) spectrum is calculated in a $\sim 860 \text{ km} \times 1300 \text{ km}$ box
 176 that does not include the coast. The data are segmented into $430 \text{ km} \times 430 \text{ km} \times 360 \text{ hour}$ bins,
 177 with 50% overlap in both time and space, resulting in a total of 77 segments for each of the two
 178 month periods March–April and August–September. The mean and linear trend in each dimension
 179 of each segment are then removed, and a 3-D Hanning window is applied before taking the 3-D
 180 Fast Fourier Transform (FFT). The Fourier transformed segments are averaged, and the squared
 181 amplitude of the average is normalized in order to satisfy Parseval’s Theorem. This results in a 3-D
 182 spectrum in k_x, k_y and ω . However, to reduce to a 2-D isotropic $\omega - k$ spectrum, the spectral energy
 183 corresponding to each $k = \sqrt{k_x^2 + k_y^2}$ is summed. The full details of this method are described by
 184 Torres et al. (2018).

185 *d. Coarse-Graining*

186 The coarse-graining method (Aluie et al. 2018) provides a framework for deriving a scale-
 187 dependent kinetic energy budget in fluid flows. The coarse-grained kinetic energy flux Π is used
 188 in this study to diagnose cross-scale kinetic energy transfer. This will provide evidence for inverse
 189 transfers following MLIs, and for a seasonally varying partition of the mesoscale energy supply
 190 from submesoscales and large scales. The cross-scale kinetic energy transfer function Π_ℓ at a scale
 191 ℓ represents the flux of kinetic energy from scales larger than ℓ to scales smaller than ℓ :

$$\Pi_\ell = -\rho_0 \bar{\mathbf{S}} : \tau_\ell, \quad (3)$$

192 where the colon represents the tensor double contraction operation, $\bar{\mathbf{S}} = (\nabla \bar{\mathbf{u}} + \nabla \bar{\mathbf{u}}^T)/2$ is the filtered
 193 strain tensor, and $\tau_\ell = \overline{\mathbf{u}\mathbf{u}} - \bar{\mathbf{u}} \bar{\mathbf{u}}$ is defined as the sub-filter stress tensor. More details about the
 194 filtering and this derivation can be found in Aluie et al. (2018).

195 The total amount of kinetic energy transferred across a given scale ℓ can be calculated by
 196 integrating Π_ℓ over the whole spatial domain D and time:

$$\Delta E_{\text{cascade}}(t) = - \int_{t_0}^t \int_D \Pi_\ell(x, y, z, t) dx dy dz dt, \quad (4)$$

197 where $\Delta E_{\text{cascade}}(t)$ represents the total amount of energy gained by scales larger than ℓ from scales
 198 smaller than ℓ over the time period from t_0 to t .

199 *e. Dynamical Filtering*

200 The dynamical filter is used in Section 3b to define submesoscale kinetic energy as a balanced
 201 component separated from internal gravity waves (IGWs) and then split by a low-pass spatial filter.
 202 A Butterworth filter at the boundary of the IGW spectrum and the balanced motions can be derived
 203 from the IGW dispersion relation. For a more detailed discussion of this method, see Torres et al.
 204 (2022). In this study, the dynamical filter is applied on a box of size $\sim 500 \text{ km} \times 1300 \text{ km}$ in the
 205 offshore region, and the balanced motions are further separated into submesoscale and mesoscale
 206 components using a 25-km low-pass filter. This scale is chosen to be of the same order as the first
 207 baroclinic Rossby radius of deformation in the region (Chelton et al. 1998).

208 *f. Geostrophic Mixed-Layer-Averaged Kinetic Energy Budget*

209 The geostrophic mixed-layer-averaged kinetic energy budget is used in Section 3c to quantify
 210 the seasonal balance between wind work per unit mixed-layer depth and ageostrophic–geostrophic
 211 energy transfer, and to relate this to the seasonal supply of energy into the mesoscale band. The
 212 budget is calculated by taking the mixed-layer average of the incompressible, rotating Boussinesq
 213 equations to generate a momentum budget, separating the velocity into geostrophic and ageostrophic
 214 components, and then taking the dot product with the geostrophic mixed-layer-averaged velocity to
 215 generate the kinetic energy budget. Starting from the incompressible rotating Boussinesq equations

$$\partial_t \mathbf{u} + \mathbf{u} \cdot \nabla \mathbf{u} = - \frac{\nabla P}{\rho_0} - f \hat{\mathbf{z}} \times \mathbf{u} + \frac{1}{\rho_0} \partial_z \tau, \quad (5)$$

216 we can average over the depth of the mixed layer, i.e, apply the operation $h^{-1} \int_{-h}^0 [\cdot] dz$ to each term
 217 in the momentum equations, resulting in

$$\frac{D\mathbf{U}}{Dt} + f\hat{\mathbf{z}} \times \mathbf{U} = -\nabla\phi + \frac{\tau_s}{\rho_0 h} + \frac{\nabla h \cdot p(-h)}{h \cdot \rho_0}. \quad (6)$$

218 Additional terms appear from the Leibniz integral rule when mixed-layer averaging. However,
 219 here we have assumed that $\partial_t h = w_b$, where w_b is defined as the vertical velocity at the base of
 220 the mixed layer, and $\vec{u}(z = -h) \approx \vec{U}$, i.e. there is no significant jump in velocity at the base of the
 221 mixed layer. Here, $\phi = \rho_0^{-1} h^{-1} \int_{-h}^0 P(x, y, z, t) dz$ as defined by Boccaletti et al. (2007).

222 Equation 6 can be split into geostrophic and ageostrophic components such that $\mathbf{U} = \mathbf{U}_g + \mathbf{U}_a$.

$$\frac{D}{Dt}(\mathbf{U}_g + \mathbf{U}_a) = -\nabla\phi - f\hat{\mathbf{z}} \times \mathbf{U}_g - f\hat{\mathbf{z}} \times \mathbf{U}_a + \frac{\tau_s}{\rho_0 h} + \frac{\nabla h \cdot p(-h)}{h \cdot \rho_0}, \quad (7)$$

223 but, from geostrophic balance $f\hat{\mathbf{z}} \times \mathbf{U}_g = -\nabla\phi$ and so

$$\frac{D}{Dt} \left(\underbrace{\mathbf{U}_g}_{(a)} + \underbrace{\mathbf{U}_a}_{(b)} \right) = \underbrace{-f\hat{\mathbf{z}} \times \mathbf{U}_a}_{(c)} + \underbrace{\frac{\tau_s}{\rho_0 h}}_{(d)} + \underbrace{\frac{\nabla h \cdot p(-h)}{h \cdot \rho_0}}_{(e)}. \quad (8)$$

224 To generate a geostrophic kinetic energy budget, this equation is dotted with \mathbf{U}_g . Applying this to
 225 term (a) gives:

$$\mathbf{U}_g \cdot \frac{D\mathbf{U}_g}{Dt} = \frac{DK_g}{Dt}, \quad (9a)$$

226 where $K_g = \frac{1}{2} |\mathbf{U}_g|^2$ is the geostrophic kinetic energy. Term (b) results in

$$\mathbf{U}_g \cdot \frac{D\mathbf{U}_a}{Dt} = \mathbf{U}_g \cdot [\partial_t \mathbf{U}_a + \mathbf{U} \cdot \nabla \mathbf{U}_a] := -\Lambda_g, \quad (9b)$$

227 where Λ_g can be interpreted as the work done by the ageostrophic acceleration to energize the
 228 geostrophic flow, or the ageostrophic-geostrophic kinetic energy transfer. For this to be consistent,
 229 $\Lambda_g = -\mathbf{U}_g \cdot D\mathbf{U}_a/Dt = \mathbf{U}_a \cdot D\mathbf{U}_g/Dt$, which can be shown to be true. For term (c)

$$-\mathbf{U}_g \cdot f\hat{\mathbf{z}} \times \mathbf{U}_a := \Gamma_g, \quad (9c)$$

230 where Γ_g is the work done by the ageostrophic vorticity on the geostrophic flow. Next, for term (d)

$$\mathbf{U}_g \cdot \frac{\boldsymbol{\tau}_s}{\rho_0 h} = W_g, \quad (9d)$$

231 where W_g is the wind work into the *geostrophic* flow per unit depth. Finally, applying the dot
232 product with \mathbf{U}_g to term (e) gives

$$\mathbf{U}_g \cdot \frac{\nabla h \cdot p(-h)}{h \cdot \rho_0} = \frac{p(-h)}{\rho_0 h} \mathbf{U}_g \cdot \nabla h. \quad (9e)$$

233 This term represents the work done by the geostrophic flow on fronts at the base of the ML.

234 So, the total budget is

$$\underbrace{\frac{DK_g}{Dt}}_{(a)} = \underbrace{\Pi_g}_{(b)+(c)} + \underbrace{W_g}_{(d)} + \underbrace{\frac{p(-h)}{\rho_0 h} \mathbf{U}_g \cdot \nabla h}_{(e)}. \quad (10)$$

235 where $\Pi_g = \Lambda_g + \Gamma_g$ represents total work done by the ageostrophic flow on the geostrophic flow,
236 or the total ageostrophic-geostrophic kinetic energy transfer. In this study we hypothesize the
237 dominant balance

$$\frac{DK_g}{Dt} = \Pi_g + W_g. \quad (11)$$

238 These two terms are good proxies for the two mechanisms outlined in this research.

239 3. Results

240 a. Seasonal Cycle

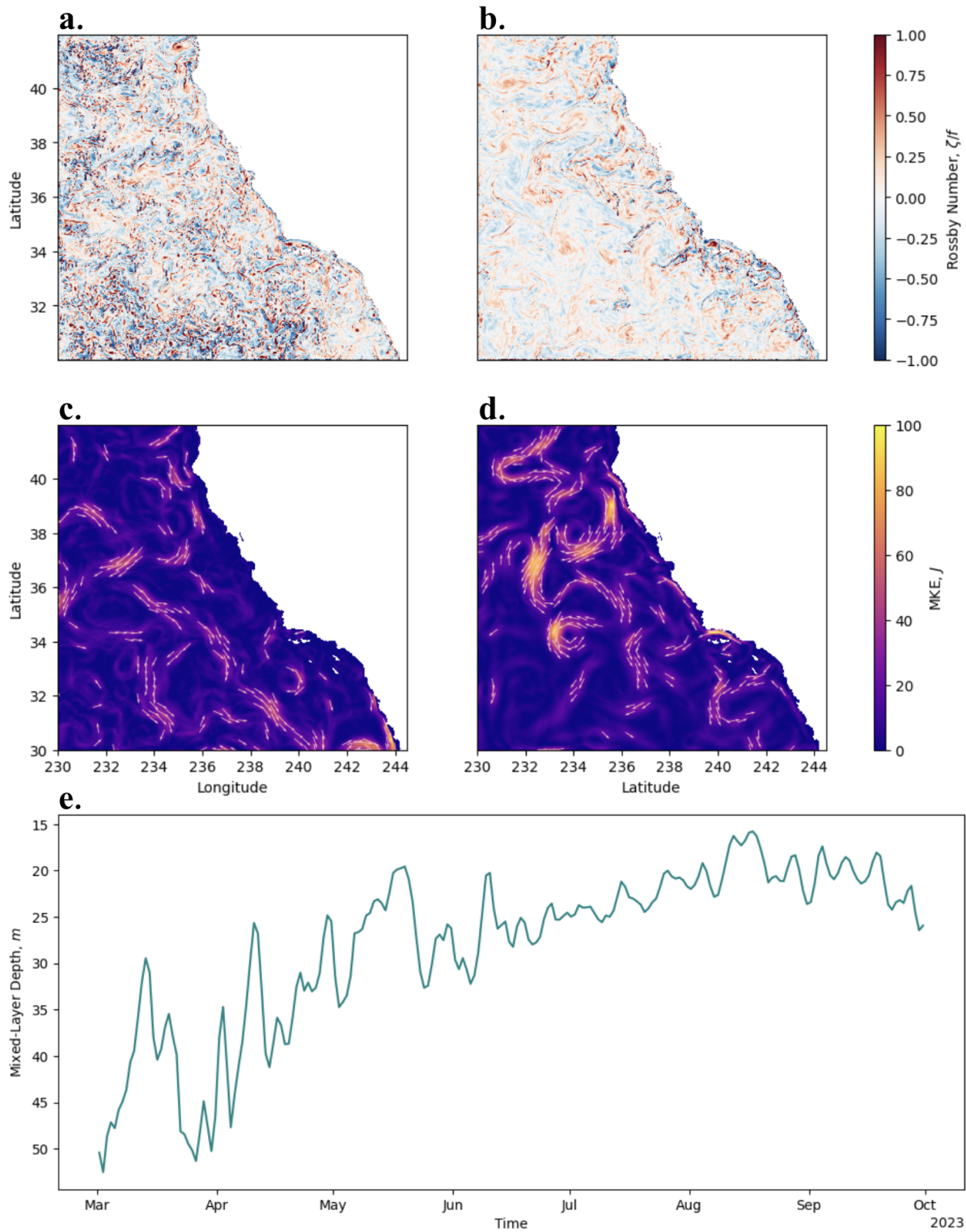
245 The surface flow of the CCS exhibits a pronounced shift in dynamical regime between late winter
246 and late summer. Figure 1a–b compares snapshots of normalized relative vorticity ζ/f at 6-m depth
247 in March and September. In early March (Fig. 1a), small, intense vortices and filaments, many
248 with $|\zeta/f| \approx O(1)$ are ubiquitous throughout the domain, indicating strong submesoscale activity,
249 particularly in the southern open-ocean region from 32–34°N. By contrast, the September field
250 (Fig. 1b) is considerably smoother; submesoscale eddies are suppressed, and the flow is dominated
251 by larger, more coherent mesoscale eddies with substantially lower $|\zeta/f|$. Seasonally averaged
252 wavenumber kinetic energy spectra also reveal strong variations in eddy scale. From winter to

253 summer, the spectral slope transitions from k^{-3} to k^{-4} , where k is the wavenumber corresponding to
254 the scale of the features, indicating a stronger submesoscale field in winter (Fig. 2a). Additionally,
255 more energy is present in the winter wavenumber spectrum at scales smaller than 25 km.

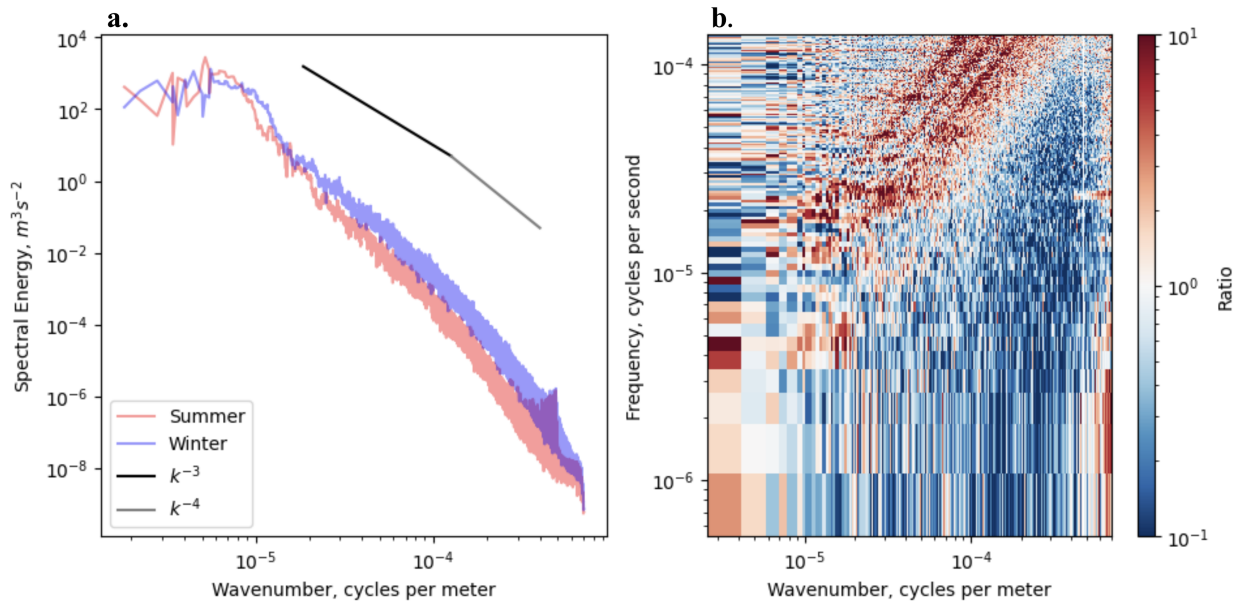
260 The mean kinetic energy (MKE) of the large-scale California Current undergoes a strong seasonal
261 cycle (Fig. 1c–d). In winter, the current is weaker and less coherent, coinciding with deeper mixed
262 layers (Fig. 1e). By contrast, in summer the current is stronger and more coherent, flowing
263 north–south as part of the North Pacific subtropical gyre. A coastal poleward return flow emerges
264 in summer that is absent in winter (Fig. 1c–d). This change is consistent with climatological
265 observations and is attributed to the seasonal upwelling cycle (Di Lorenzo 2003). These results
266 suggest a pronounced regime shift between winter and summer. Fig. 2b shows that both the largest
267 spatiotemporal scales and the internal gravity waves (IGWs) are more energetic during the summer
268 months (red), whereas the submesoscale balanced motions are more intense in winter (blue). In
269 winter, intense high-Rossby number submesoscale eddies dominate the domain (Fig. 1a), the large-
270 scale current is weak (Fig. 1b), and the mixed layer is deep and highly variable (Fig. 1e). In summer,
271 the flow is instead characterized by smooth, large-scale, low–Rossby number eddies (Fig. 1b), an
272 intensified boundary current (Fig. 1d), and a shallow mixed layer (Fig. 1e). Thus, eddies in the
273 CCS are generally small in winter and large in summer, a result of the opposing seasonal cycles
274 of submesoscale and mesoscale kinetic energies. The existence of these two contrasting states
275 suggests that the upper ocean is not governed by a single forcing process year-round, but is instead
276 forced by multiple mechanisms, which each vary seasonally. In particular, the marked differences
277 in eddy scale, Rossby number, and mixed-layer depth imply that the mesoscale circulation is
278 maintained by distinct forcing pathways at different points in the seasonal cycle.

279 *b. Mixed-Layer Instabilities in the CCS*

280 Mixed-layer instabilities are a mechanism that transfers buoyancy vertically for restratification
281 (Boccaletti et al. 2007). In this study, we hypothesize that the seasonal cycle in CCS submesoscale
282 kinetic energy is strongly modulated by mixed-layer instabilities that generate submesoscale eddies.



241 FIG. 1. Instantaneous Rossby number at 6-m depth on 1 March 2023, 16:00 (a) and 30 September 2023, 16:00
 242 (b). Monthly mean surface kinetic energy for March (c) and September (d), with velocity vectors plotted where
 243 mean kinetic energy exceeds 75 J to illustrate the California Current System. (e) Daily mean mixed-layer depth
 244 for the full study period.

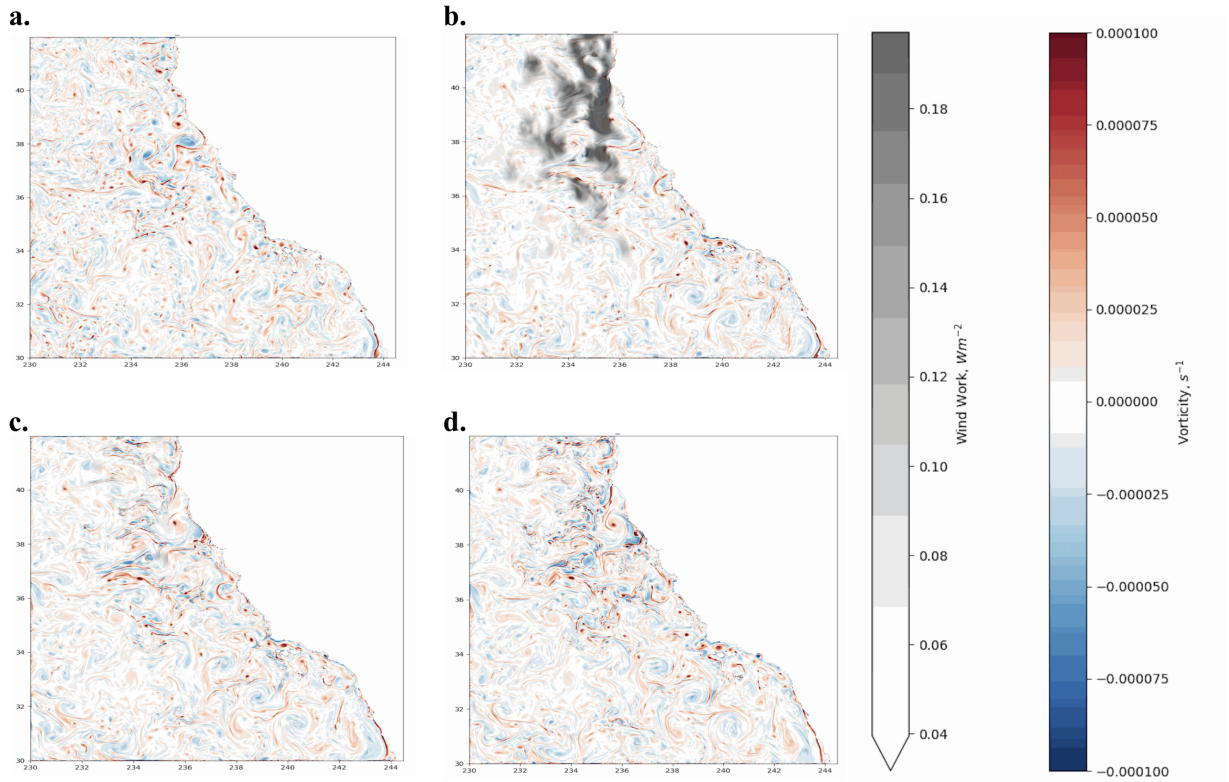


256 FIG. 2. a. Wavenumber KE spectra calculated in the region 230–235°E and 30–42°N for the time periods
 257 March–April (blue) and August–September (red), and spectral slopes of k^{-3} (black) and k^{-4} (gray). b. The
 258 ratio of March–April to August–September wavenumber–frequency KE spectra, where red represents enhanced
 259 energy in summer and blue represents enhanced energy in winter.

283 1) MLI CASE STUDY

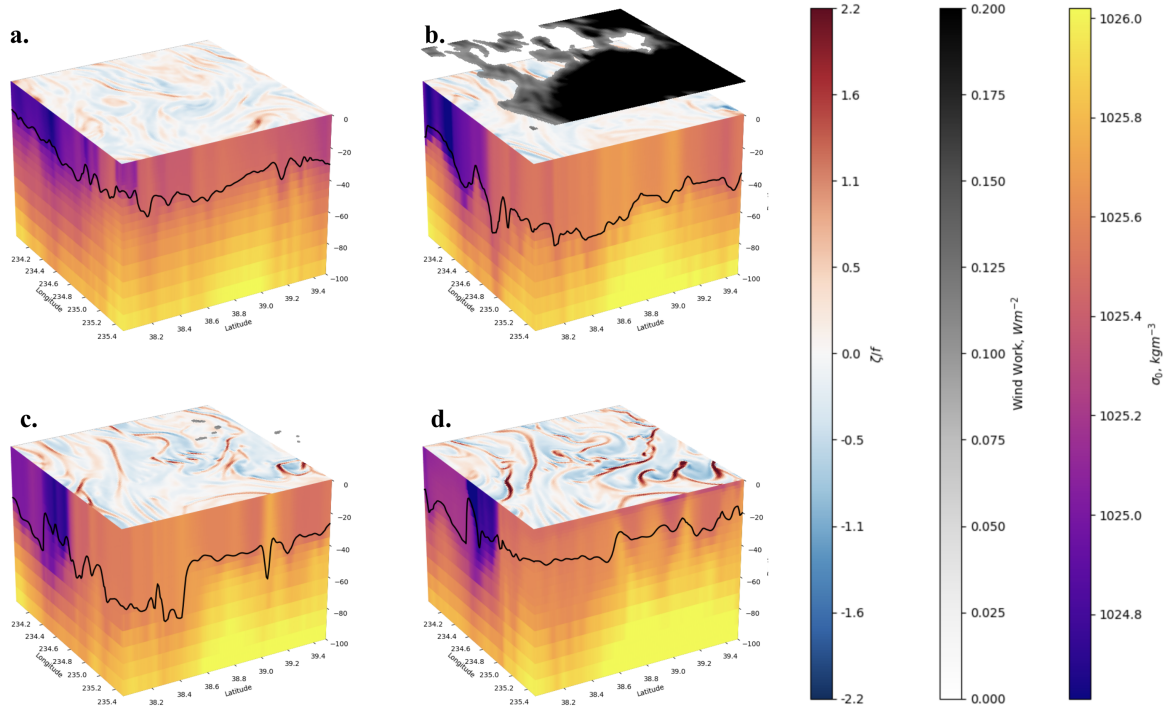
286 To illustrate the full spatio-temporal development of a single mixed-layer instability event,
 287 Figures 3–5 focus on a region of exceptionally strong storm forcing during 19–27 May 2023.
 288 Prior to the storm, the flow is dominated by moderate mesoscale variability with relatively weak
 289 submesoscale vorticity (Fig. 3a, 4a). This is followed by the passage of a strong storm (Fig. 3b, 4b),
 290 which induces intense small-scale lateral buoyancy gradients and deepens the mixed layer by 20–
 291 25m (Fig. 3c, 4c). This, in turn, results in a burst of submesoscale activity four days later, driven
 292 by frontal mixed-layer instabilities (Fig. 3d, 4d).

295 Averaging over the full domain can obscure the signal of mixed-layer instabilities, as these
 296 processes represent localized responses to mixed-layer deepening and subsequent restratification.
 297 Focusing on the subregion where nearly all grid points experience storm-level wind forcing (Fig. 4b)
 298 allows for the construction of a more representative time series based on spatial means over this
 299 smaller domain. Figure 5 presents spatially averaged diagnostics for this subregion as a function

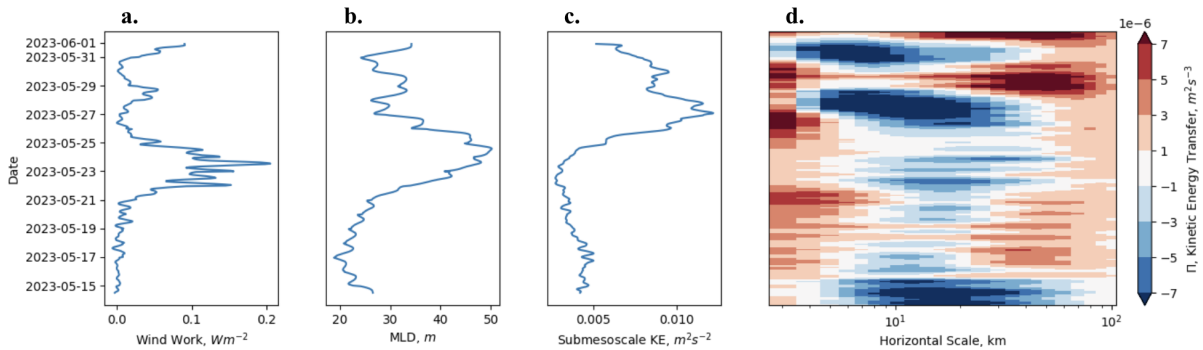


284 FIG. 3. Daily mean vorticity at 6 m, with wind work greater than 0.05 W m^{-2} overlaid in gray on a. 19 May
 285 2023 b. 23 May 2023 c. 25 May 2023 d. 27 May 2023

300 of time. Wind work (Fig. 5a) is followed by a deepening of the mixed-layer (Fig. 5b) with a
 301 lag of approximately one day. Strong wind work is hypothesized to deepen the mixed layer by
 302 providing the mechanical energy necessary for mixing, and via buoyancy loss to the atmosphere.
 303 Subsequently, the mixed layer restratifies (Fig. 5b, after May 28). This restratification is associated
 304 with the generation of submesoscale currents, represented here as submesoscale kinetic energy,
 305 which peaks approximately four days after the storm-induced wind work (Fig. 5c). The peak
 306 submesoscale kinetic energy is further characterized in Figure 5d as energy injection at, and
 307 divergence from, scales of approximately 4 km. A portion of this energy cascades downscale
 308 to dissipate, while another portion undergoes an inverse cascade, merging into larger eddies and
 309 energizing the mesoscale field at scales up to 50 km (Fig. 5d). Taken together, these results suggest
 310 the hypothesis that mixed-layer instabilities serve as a mechanism by which submesoscale energy
 311 is transferred into the mesoscale, with a lag of a few days following the initial storm event.



293 FIG. 4. Snapshots of vorticity at 6 m, with wind work greater than 0.1 W m^{-2} overlaid in gray on a. 22:00, 20
 294 May 2023 b. 11:00, 23 May 2023 c. 11:00, 25 May 2023 d. 00:00, 27 May 2023



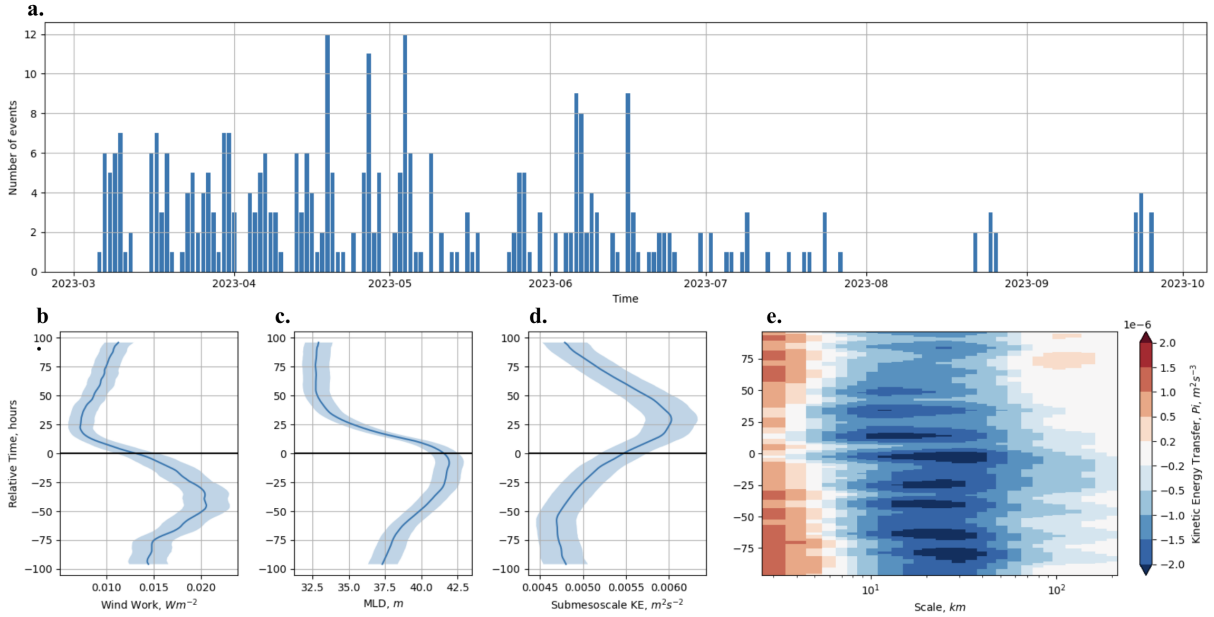
312 FIG. 5. Spatial mean over $234\text{-}235.5^\circ \text{ E}$ and $38\text{-}39.5^\circ \text{ N}$ of a. wind work, b. mixed-layer depth as defined by
 313 the potential energy anomaly in Section 2b, c. submesoscale kinetic energy, defined by a dynamical filter that
 314 removes the IGWs defined in Section 2e and a subsequent 25-km high-pass filter, d. the kinetic energy transfer
 315 function, Π , defined using the coarse-graining method outlined in Section 2d. Positive values indicate downscale
 316 kinetic energy transfer.

317 2) COMPOSITE ANALYSIS OF MLIs IN THE CCS

318 These deepening–restratification sequences occur throughout the time series but are most com-
319 mon and energetic during late winter and early spring, coinciding with the period of deepest
320 mixed layers and strongest absolute wind forcing. To isolate the general statistical behavior of
321 these events, we construct a composite analysis for mixed-layer instabilities. We first compute the
322 change in MLD over 5-hour periods, and then extract the most negative 1% of this variable to
323 represent the strongest restratification events. We then screen these events to satisfy the additional
324 conditions: (a) the event center is a maximum in a spatio-temporal cylinder of spatial radius 30 km
325 and temporal radius 120 hours, and (b) any events that share the same geographic center must be
326 separated by at least 120 hours in time. These criteria were chosen to align with the definition
327 of MLIs used by Boccaletti et al. (2007) as a mechanism for restratification of the mixed layer,
328 and to ensure that individual events are sufficiently separated in time and space to be treated as
329 independent realizations. Once events are selected, they are composite averaged.

330 Figure 6a shows the distribution of the 336 events in the domain spanning 230–236°E and 35–
331 40°N over the 7-month time series. The events are heavily concentrated during winter and spring
332 and are subdued in summer, although not completely absent. Figures 6b–e show the same bulk
333 statistic means as considered in the case study event in Figure 5. The bulk statistics show a similar
334 progression to the example shown in Figure 5, except with a less extreme MLD variation and a
335 compressed time-span. The composite and the individual example reveal several features consistent
336 with the canonical MLI cycle described in earlier studies (Boccaletti et al. 2007; Fox-Kemper et al.
337 2008). Here, strong winds (Fig. 6b) result in a deepening of the mixed layer, which reaches its
338 deepest values within 1–2 inertial periods (1 day) after the peak wind work (Fig. 6c). A sharp peak
339 in submesoscale kinetic energy emerges with a delay of 1 day (Fig. 6d). Concurrent with the peak
340 submesoscale kinetic energy is a decreased dominant energy injection scale and a strong inverse
341 cascade at smaller scales (Fig. 6e). As this energy cascades upscale, the submesoscale kinetic
342 energy decreases.

349 Both the composite (Fig. 6) and the case study (Figs. 3–5) demonstrate that mixed-layer deepening
350 events in the CCS are commonly followed by enhanced submesoscale activity and restratification
351 consistent with MLI dynamics. These events occur throughout the year but cluster in periods
352 of deeper mixed layers, consistent with the hypothesis that the elevated wintertime submesoscale



343 FIG. 6. a. Temporal distribution of mixed-layer instability events included in composite. Composite means
 344 over a radius of 30km around the event center with shading indicating the 95% bootstrapped confidence interval
 345 of b. wind work, c. mixed-layer depth, defined by the potential energy anomaly in Section 2b, d. submesoscale
 346 kinetic energy, defined by a dynamical filter that removes the IGWs and a subsequent 25-km high-pass filter.
 347 Composite disk-mean of e. the kinetic energy transfer function, Π , defined using the coarse-graining method
 348 outlined in Section 2d

353 kinetic energy shown in Section 3a is due to enhanced MLIs. Their cumulative effect, and the
 354 seasonal changes in their frequency and intensity, underpin the seasonal cycles of submesoscale
 355 kinetic energy, mesoscale kinetic energy, and their exchange, which we quantify in Section 3c.

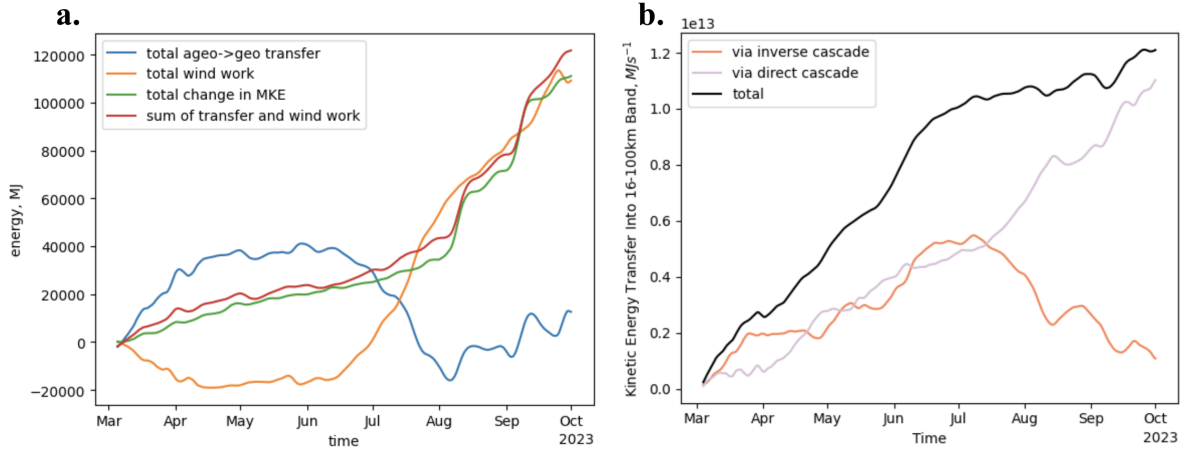
356 *c. Momentum Trapping and Baroclinic Instability*

357 Figure 1c–d highlights a pronounced seasonal contrast in the mean kinetic energy, with substan-
 358 tially stronger currents during summer. A plausible explanation for this behavior is momentum
 359 trapping (Peng et al. 2022), whereby increased upper-ocean stratification confines wind-driven mo-
 360 mentum to a shallower mixed layer, reducing the effective inertia of the forced layer and allowing
 361 the same wind stress to generate faster currents.

362 Figure 7a shows the time-integrated terms of the geostrophic kinetic energy budget described
363 in Section 2f. The ageostrophic-to-geostrophic transfer term (blue line) provides a measure of
364 the inverse transfer of energy from mixed-layer instabilities and other ageostrophic motions into
365 geostrophic mesoscale and current-scale flows. This transfer increases through spring (March–
366 May) and peaks in early summer (June), coincident with the period when mixed-layer instabilities
367 rapidly decline in frequency (Fig. 6a). Beyond this point, the sign reversal of the transfer indicates
368 a regime shift in which ageostrophic motions act as a net sink of geostrophic kinetic energy rather
369 than a source.

370 In contrast, the cumulative wind work per unit mixed-layer depth (orange line in Fig. 7a)
371 increases steadily from early summer onward, despite a decrease in the absolute wind work as
372 the year progresses. Cumulative wind work becomes the leading-order contributor to changes
373 in kinetic energy during the shallow mixed layer season (July–October). The close agreement
374 between the sum of wind work and ageostrophic–geostrophic transfer (red line) and the diagnosed
375 change in kinetic energy (green line) demonstrates that these terms dominate the seasonal budget.
376 Importantly, during summer the balance is overwhelmingly controlled by wind work, consistent
377 with the momentum-trapping hypothesis: as the mixed layer shoals, wind stress becomes a more
378 efficient pathway for energy input, accelerating the mixed-layer current and strengthening the
379 large-scale flow. In summer, enhanced stratification strengthens the large-scale current, increasing
380 the energy available for transfer to the mesoscale. Figure 7b shows the cumulative kinetic energy
381 transfer (defined by equation 4) into the 16–100-km band, decomposed by source scale using the
382 coarse-grained energy flux Π . The mesoscale band was chosen to be 16–100 km based on the
383 maximum cumulative kinetic energy transfer from submesoscales up into the mesoscale (16 km)
384 and from the large-scale current system downscale into the mesoscale (100 km). Energy transferred
385 from submesoscales (orange line in Figure 7b) increases through spring and peaks in early summer,
386 consistent with active mixed-layer instabilities, but subsequently weakens as enhanced stratification
387 suppresses mixed-layer instability generation. Energy transferred from the large-scale flow (purple
388 line) increases steadily throughout the year and exhibits a marked increase in slope around July,
389 implying a more efficient downscale transfer into the mesoscale during summer.

390 This behavior suggests a transition in the dominant pathway supplying mesoscale kinetic energy:
391 from an inverse transfer driven by submesoscale mixed-layer instabilities in spring to a strengthened
392



370 FIG. 7. a. 4-day running mean of time-integrated terms in the geostrophic mixed-layer averaged budget averaged
 371 over the domain spanning $35.5\text{--}39.5^\circ\text{N}$ and $231\text{--}235^\circ\text{E}$: total transfer from ageostrophic motions to geostrophic
 372 motions Π_g (blue), total wind work into the ocean per unit depth W_g (orange), sum of both ageostrophic to
 373 geostrophic energy transfer and wind work $\Pi_g + W_g$ (red) and change in geostrophic kinetic energy DK_g/Dt
 374 (green). b. integrated kinetic energy transfer function into the 16-100-km band averaged over $230\text{--}235^\circ\text{E}$ and
 375 $30\text{--}42^\circ\text{N}$ from scales $>100\text{ km}$ (purple) and scales $<16\text{ km}$ (orange), and their sum (black).

398 direct transfer from the intensified large-scale current in summer. The strengthened current is
 399 associated with enhanced horizontal strain, promoting mesoscale baroclinic instability that converts
 400 large-scale kinetic energy into mesoscale eddies. The persistence and acceleration of the large-
 401 scale-to-mesoscale transfer despite declining submesoscale input highlights the central role of the
 402 summer mean flow in maintaining mesoscale activity.

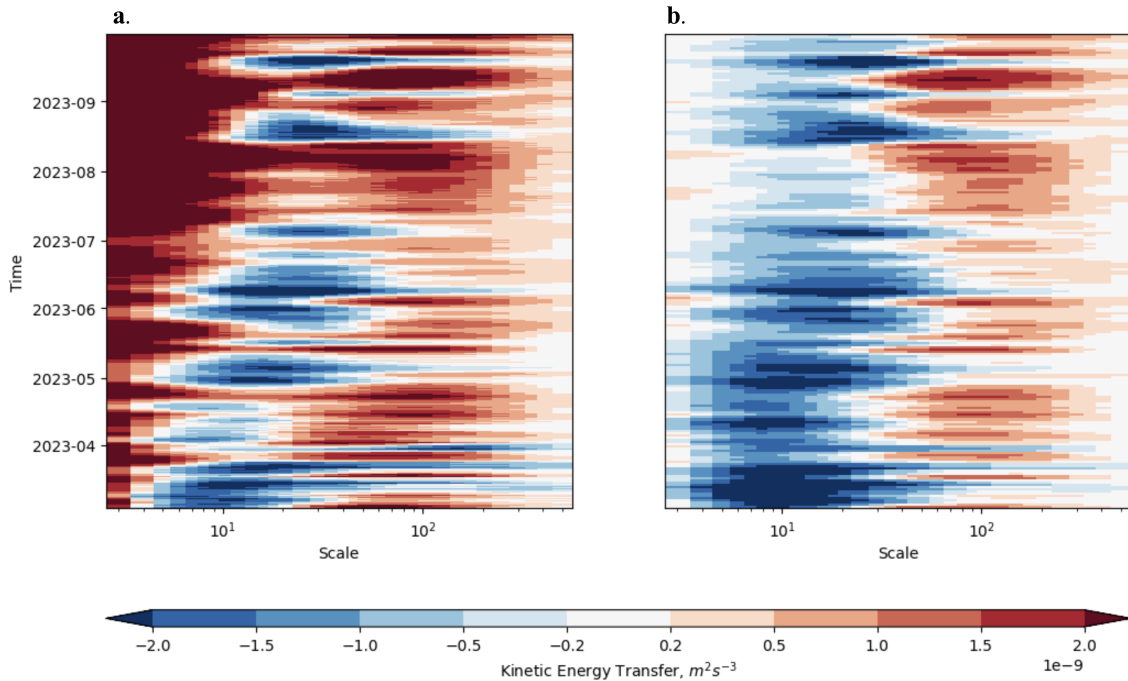
403 *d. Two Pathways to Mesoscale Kinetic Energy*

404 The results presented in Sections 3b and 3c indicate that mesoscale eddies in the CCS are
 405 energized by two dynamically distinct pathways whose relative importance varies seasonally:
 406 an inverse transfer from submesoscales driven by mixed-layer instabilities during winter and
 407 spring, and a direct transfer from the intensified large-scale flow during summer, consistent with
 408 mesoscale baroclinic instability. Previous studies have established that both submesoscale mixed-
 409 layer instabilities and mesoscale baroclinic instability are active in boundary current systems
 410 (Boccaletti et al. 2007; Capet et al. 2008a; Rocha et al. 2016), and have suggested that MLIs can

411 contribute to mesoscale variability through upscale energy transfer (Capet et al. 2008a; Schubert
412 et al. 2020; Sasaki et al. 2014). However, the seasonal variation in relative importance of these
413 processes, and how they jointly shape the mesoscale energy budget in the CCS, has remained less
414 clearly quantified.

415 Figure 7b directly quantifies the seasonal partition of energy supply into the mesoscale band using
416 the coarse-grained flux Π , decomposed by source scale. Energy transferred from submesoscales
417 (< 16 km) increases through spring and peaks in early summer, consistent with active mixed-layer
418 instabilities and the composite evolution described in Section 3b: mixed-layer deepening events
419 generate intense submesoscale eddies which subsequently merge through an inverse cascade,
420 transferring energy upscale into the mesoscale band (Capet et al. 2008a; Schubert et al. 2020;
421 Sasaki et al. 2014). In contrast, energy transferred from the large-scale flow (> 100 km) increases
422 steadily throughout the year and exhibits a marked increase in slope around July, indicating the onset
423 of a more efficient downscale transfer into the mesoscale during summer. This timing coincides
424 with the shallow mixed-layer season (Fig. 1e) and with the increasing importance of wind work
425 per unit mixed-layer depth in the geostrophic budget (Fig. 7a), consistent with momentum trapping
426 (Peng et al. 2022) strengthening the large-scale flow and increasing the energy available for transfer
427 to the mesoscale.

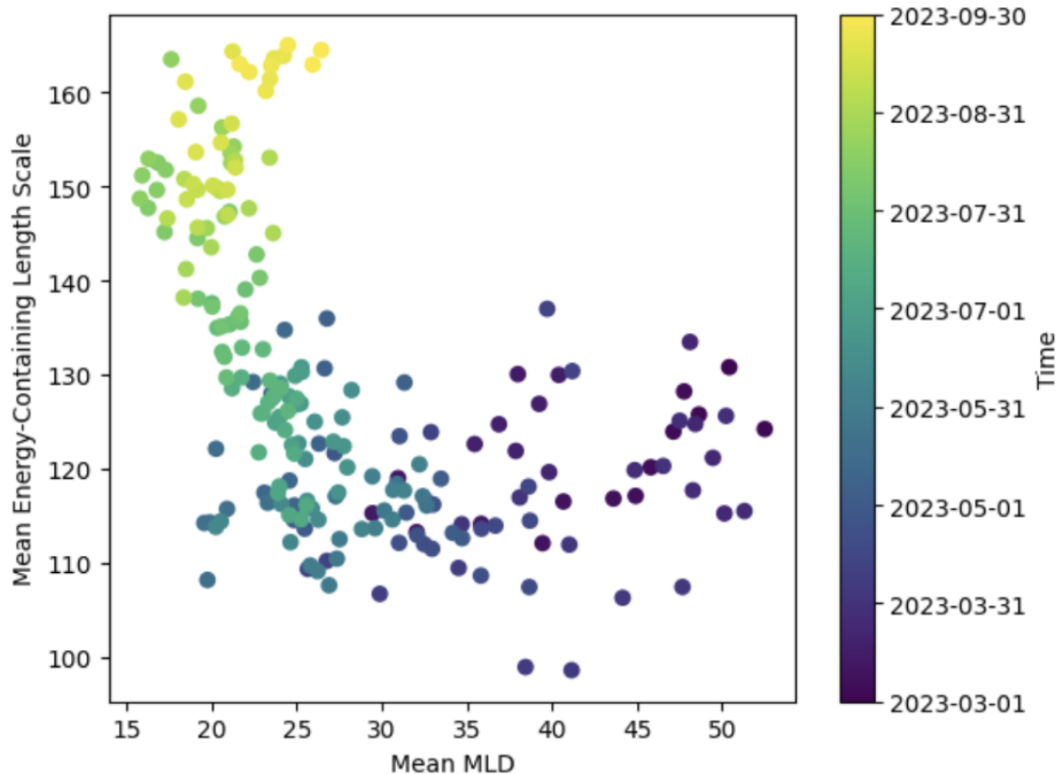
430 The seasonal transition in the dominant source is also evident in the full, time-scale evolution of
431 Π (Fig. 8a). During winter and spring, Π exhibits frequent, patchy negative anomalies representing
432 inverse cascades, consistent with intermittent but intense upscale transfer associated with restrat-
433 ification events and mixed-layer instabilities. These events become less frequent and weaker in
434 summer, coincident with the suppression of submesoscale activity. With the lack of a small-scale
435 energy injection scale in summer, the direct cascade to dissipation extends up to larger scales and
436 is part of the reason for the submesoscale becoming a sink for the mesoscale rather than a source.
437 Consistent with Tedesco et al. (2023), we find that daily averaging largely suppresses the direct cas-
438 cade to dissipation (Fig. 8b), indicating that a substantial fraction of the turbulent energy transfer to
439 dissipative scales resides at high temporal frequencies. Persistent positive Π anomalies are present
440 at scales of 100–200 km, but they intensify as the year goes on, reflecting a strengthening direct
441 cascade from the mean current and large mesoscale features into the mesoscale band. Together,
442 Figures 7b and 8 show a convergence of energy into the mesoscale band from both larger and



428 FIG. 8. A 72-hour rolling average of the mean kinetic energy transfer function, Π , averaged over 230–235° E
 429 and 30–42° N using a) hourly data and b) daily-averaged data

443 smaller scales, with the source partitioning shifting from predominantly submesoscale in spring to
 444 predominantly large-scale in summer.

447 This source shift provides a natural interpretation of the seasonal change in characteristic eddy
 448 scale. Figure 9 shows the mean energy-containing eddy scale, computed as the integral over the
 449 variance-preserving wavenumber spectrum, plotted against the domain-mean mixed-layer depth.
 450 During winter and spring (purple and blue dots), the two quantities are not related, reflecting
 451 a regime in which mesoscale variability is energized from smaller scales by an inverse cascade
 452 that is largely controlled by intermittent, local restratification events. Beginning in early summer
 453 (green and yellow dots), however, the two become tightly correlated, with shoaling mixed layers
 454 associated with a systematic increase in eddy scale. This transition coincides with the onset of
 455 strong momentum trapping (Section 3c), whereby wind-driven energy input becomes increasingly
 456 confined to the shallow mixed layer, amplifying the large-scale current. The intensified current
 457 strengthens lateral buoyancy gradients and horizontal strain, promoting mesoscale baroclinic in-



445 FIG. 9. Daily mean energy containing length scale, calculated as the integral over the variance-preserving
 446 wavenumber spectrum vs daily mean mixed-layer depth.

458 stability that directly transfers kinetic energy from the mean flow to the mesoscale eddies while
 459 acting to relax buoyancy gradients imposed by the straining flow.

460 4. Discussion and Conclusion

461 This study has quantified the seasonal mechanisms that supply kinetic energy to the mesoscale
 462 band $O(100 \text{ km})$ in the California Current System, using a high-resolution simulation and a suite
 463 of energetics diagnostics. The results show that the CCS mesoscale band is maintained through
 464 two dynamically distinct pathways whose relative importance shifts over the seasonal cycle: an
 465 inverse transfer from submesoscales associated with mixed-layer instabilities during winter and
 466 spring, and a direct transfer from the intensified large-scale flow during summer.

467 An important implication is that the mesoscale band in the CCS functions as an intermediate
 468 reservoir that can be supplied by energy from both smaller and larger scales, with the balance

469 between these sources varying seasonally. This behavior is consistent with theoretical expectations
470 for geostrophic turbulence in which both upscale and downscale transfers may coexist depending
471 on the structure of forcing and dissipation (Vallis 2017; Aluie et al. 2018). It also helps reconcile
472 two previously emphasized perspectives in the literature: one in which mesoscale variability is
473 influenced by submesoscale mixed-layer processes (Boccaletti et al. 2007; Capet et al. 2008a;
474 Rocha et al. 2016), and another in which mesoscale energy is primarily derived from instabilities
475 of the large-scale circulation (Vallis 2017). In the CCS, both pathways are active, but their relative
476 roles depend strongly on seasonal stratification and mixed-layer depth. The framework developed
477 here therefore provides a basis for interpreting seasonal mesoscale variability in terms of underlying
478 energy pathways, and for comparative application to other boundary current systems where mixed-
479 layer depth and storm forcing vary strongly over the seasonal cycle (Rocha et al. 2016; Brannigan
480 et al. 2015; Qiu et al. 2014; Sasaki et al. 2014). A further goal is to identify whether a critical
481 mixed-layer depth or stratification threshold governs the regime shift between submesoscale-driven
482 inverse transfer and large-scale-driven direct transfer.

483 The results presented here also suggest that mesoscale variability in the CCS may be sensitive to
484 long-term changes in stratification and atmospheric forcing. Increased upper-ocean stratification
485 associated with surface warming would favor shallower mixed layers and potentially enhance the
486 efficiency of momentum trapping, strengthening the large-scale pathway for mesoscale energiza-
487 tion. Conversely, changes in storm frequency or intensity would be expected to modulate the
488 prevalence of deepening–restratification events and therefore the contribution of the MLI path-
489 way. For the North Pacific, potential changes in large-scale atmospheric circulation may therefore
490 influence mesoscale variability in the CCS by changing the frequency and intensity of deepening–
491 restratification events due to storms—and hence the relative contribution of the two pathways
492 outlined in this research. Understanding how these competing effects evolve under climate change
493 remains an open question.

494 Recent observations from the Sub-Mesoscale Ocean Dynamics Experiment (S-MODE) provide
495 an important observational context for the mechanisms identified here. The presence of an ener-
496 getic field of submesoscale fronts, filaments, and vortices in the California Current region west
497 of central California was reported, demonstrating that the upper ocean supports vigorous subme-
498 soscale variability embedded within a broader mesoscale circulation (Farrar et al. 2025). Airborne

499 DopplerScatt measurements during S-MODE revealed rapidly evolving 1–20 km features with
500 Rossby number and divergence normalized by the Coriolis frequency of order unity and inferred
501 vertical velocities exceeding 200 m day^{-1} at tens of meters depth (Torres et al. 2024). These
502 observations are qualitatively consistent with the winter–spring regime identified here, in which
503 deep mixed layers and storm-driven forcing favor mixed-layer instabilities that inject energy at
504 submesoscales, resulting in a vigorous submesoscale field. However, the results from DopplerScatt
505 suggest a more energetic submesoscale field with a spectral slope of $\sim k^{-2}$ compared with this study
506 in which we find a $\sim k^{-3}$ slope. We hypothesize that the disagreement in spectral slope occurs be-
507 cause the DopplerScatt measurements are higher resolution and resolve more of the submesoscale
508 field. Subgridscale submesoscale motions in the model could therefore be underrepresented in the
509 simulated velocity field, and their omission may lead to an underestimate of the magnitude of the
510 inverse kinetic energy transfer from submesoscales into the mesoscale band. The contribution of
511 mixed-layer instabilities to the mesoscale kinetic energy budget inferred here may represent a lower
512 bound. Future work could combine DopplerScatt velocity measurements with coarse-grained ki-
513 netic energy diagnostics to directly quantify cross-scale energy transfers at smaller spatial scales
514 and assess their contribution to mesoscale energization in the California Current System. Potential
515 future DopplerScatt flights could represent an opportunity to further quantify the contribution of
516 submesoscale motions to the mesoscale kinetic energy band.

517 Quantifying the balance between upscale and downscale cascades under different forcing regimes
518 may help resolve long-standing questions about energy transfer in the ocean. The framework
519 presented here could be applied to other systems, such as the Kuroshio Extension, Gulf Stream,
520 or the Antarctic Circumpolar Current, where the seasonal cycle of stratification or storms are also
521 important. Based on the results of this study, we hypothesize that in more energetic Western
522 boundary current systems, the MLI pathway will be enhanced, particularly in areas with high
523 variance in stratification.

524 *Acknowledgments.* We thank Dr. Hector Torres for providing code for dynamical filtering,
525 JFG and STG acknowledge support from NASA contract 80GSFC24CA067. JFG, STG, and
526 SPX were also supported through a subaward from Remote Sensing Systems for NASA award
527 80NSSC22M0010. STG also acknowledged support from NASA awards 80NSSC21K1822 and
528 80NSSC24K1657. LS acknowledges support from NASA grant 80NSSC24K1653. ACNG ac-
529 knowledges support from the UK Natural Environment Research Council (grant NE/W009501/1).
530 JM and JA acknowledge funding by the Naval Research Laboratory base program Ocean Subme-
531 soscale Eddy Evolution. This paper is contribution NRL/7320/JA–2026/3 and has been approved
532 for public release.

533 *Data availability statement.* Processed intermediate data files are available through the UC San
534 Diego Library Digital Collections (DOI: <https://doi.org/10.6075/J0DF6S64>), along with the code
535 used to generate the figures in this study. The intermediate files primarily consist of variables
536 extracted from the raw NCOM output, in some cases with additional temporal averaging or derived
537 calculations required for figure generation. Details of the processing, averaging, and derived
538 quantities are provided in the accompanying README file.

539 **References**

540 Allard, R., E. Rogers, P. Martin, T. Jensen, and P. Chu, 2015: The US Navy Coupled Ocean-Wave
541 Prediction System. *Oceanography*, **27** (3), 92–102, <https://doi.org/10.5670/oceanog.2014.71>,
542 URL <https://tos.org/oceanography/article/the-us-navy-coupled-ocean-wave-prediction-system>.

543 Aluie, H., M. Hecht, and G. K. Vallis, 2018: Mapping the Energy Cascade in the North At-
544 lantic Ocean: The Coarse-Graining Approach. *Journal of Physical Oceanography*, **48** (2),
545 225–244, <https://doi.org/10.1175/JPO-D-17-0100.1>, URL <https://journals.ametsoc.org/view/journals/phoc/48/2/jpo-d-17-0100.1.xml>.

547 Asselin, O., and W. R. Young, 2020: Penetration of Wind-Generated Near-Inertial
548 Waves into a Turbulent Ocean. *Journal of Physical Oceanography*, **50** (6), 1699–1716,
549 <https://doi.org/10.1175/JPO-D-19-0319.1>, URL <https://journals.ametsoc.org/view/journals/phoc/50/6/JPO-D-19-0319.1.xml>.

- 551 Barron, C. N., A. B. Kara, P. J. Martin, R. C. Rhodes, and L. F. Smedstad, 2006: Formulation,
552 implementation and examination of vertical coordinate choices in the Global Navy Coastal
553 Ocean Model (NCOM). *Ocean Modelling*, **11** (3), 347–375, [https://doi.org/10.1016/j.ocemod.](https://doi.org/10.1016/j.ocemod.2005.01.004)
554 2005.01.004, URL <https://www.sciencedirect.com/science/article/pii/S1463500305000120>.
- 555 Barron, C. N., and L. F. Smedstad, 2002: Global river inflow with Navy Coastal Ocean Model.
556 *OCEANS'02 MTS/IEEE*, IEEE, Vol. 3, 1472–1479, URL [https://ieeexplore.ieee.org/abstract/](https://ieeexplore.ieee.org/abstract/document/1191855/)
557 [document/1191855/](https://ieeexplore.ieee.org/abstract/document/1191855/).
- 558 Boccaletti, G., R. Ferrari, and B. Fox-Kemper, 2007: Mixed Layer Instabilities and Restratification.
559 *Journal of Physical Oceanography*, **37** (9), 2228–2250, <https://doi.org/10.1175/JPO3101.1>,
560 URL <https://journals.ametsoc.org/view/journals/phoc/37/9/jpo3101.1.xml>.
- 561 Brannigan, L., D. P. Marshall, A. Naveira-Garabato, and A. J. George Nurser, 2015: The seasonal
562 cycle of submesoscale flows. *Ocean Modelling*, **92**, 69–84, [https://doi.org/10.1016/j.ocemod.](https://doi.org/10.1016/j.ocemod.2015.05.002)
563 2015.05.002, URL <https://www.sciencedirect.com/science/article/pii/S1463500315000803>.
- 564 Buckingham, C. E., and Coauthors, 2016: Seasonality of submesoscale flows in the ocean sur-
565 face boundary layer. *Geophysical Research Letters*, **43** (5), 2118–2126, [https://doi.org/10.1002/](https://doi.org/10.1002/2016GL068009)
566 2016GL068009, URL <https://onlinelibrary.wiley.com/doi/abs/10.1002/2016GL068009>.
- 567 Callies, J., R. Ferrari, J. M. Klymak, and J. Gula, 2015: Seasonality in submesoscale tur-
568 bulence. *Nature Communications*, **6**, <https://doi.org/DOI:10.1038/ncomms7862>, URL [https://](https://www.nature.com/articles/ncomms7862)
569 www.nature.com/articles/ncomms7862.
- 570 Capet, X., J. C. McWilliams, M. J. Molemaker, and A. F. Shchepetkin, 2008a: Mesoscale
571 to Submesoscale Transition in the California Current System. Part I: Flow Structure,
572 Eddy Flux, and Observational Tests. *Journal of Physical Oceanography*, **38** (1), 29–43,
573 <https://doi.org/10.1175/2007JPO3671.1>, URL [https://journals.ametsoc.org/view/journals/phoc/](https://journals.ametsoc.org/view/journals/phoc/38/1/2007jpo3671.1.xml)
574 [38/1/2007jpo3671.1.xml](https://journals.ametsoc.org/view/journals/phoc/38/1/2007jpo3671.1.xml).
- 575 Capet, X., J. C. McWilliams, M. J. Molemaker, and A. F. Shchepetkin, 2008b: Mesoscale to
576 Submesoscale Transition in the California Current System. Part II: Frontal Processes. *Journal*
577 *of Physical Oceanography*, **38** (1), 44–64, <https://doi.org/10.1175/2007JPO3672.1>, URL [https://](https://journals.ametsoc.org/view/journals/phoc/38/1/2007jpo3672.1.xml)
578 journals.ametsoc.org/view/journals/phoc/38/1/2007jpo3672.1.xml.

- 579 Charney, J. G., 1971: Geostrophic Turbulence. *Journal of the Atmospheric Sciences*, **28** (6), 1087–
580 1095, [https://doi.org/10.1175/1520-0469\(1971\)028<1087:GT>2.0.CO;2](https://doi.org/10.1175/1520-0469(1971)028<1087:GT>2.0.CO;2), URL [https://journals.
581 ametsoc.org/view/journals/atsc/28/6/1520-0469_1971_028_1087_gt_2_0_co_2.xml](https://journals.ametsoc.org/view/journals/atsc/28/6/1520-0469_1971_028_1087_gt_2_0_co_2.xml).
- 582 Chelton, D. B., R. A. deSzoeko, M. G. Schlax, K. E. Naggar, and N. Siwertz, 1998: Geographical
583 Variability of the First Baroclinic Rossby Radius of Deformation. *Journal of Physical Oceanog-
584 raphy*, **28** (3), 433–460, [https://doi.org/10.1175/1520-0485\(1998\)028<0433:GVOTFB>2.0.
585 CO;2](https://doi.org/10.1175/1520-0485(1998)028<0433:GVOTFB>2.0.CO;2), URL [https://journals.ametsoc.org/view/journals/phoc/28/3/1520-0485_1998_028_0433_
586 gvotfb_2.0.co_2.xml](https://journals.ametsoc.org/view/journals/phoc/28/3/1520-0485_1998_028_0433_gvotfb_2.0.co_2.xml).
- 587 Cummings, J. A., 2005: Operational multivariate ocean data assimilation. *Quarterly Journal of the
588 Royal Meteorological Society*, **131** (613), 3583–3604, <https://doi.org/10.1256/qj.05.105>, URL
589 <https://onlinelibrary.wiley.com/doi/abs/10.1256/qj.05.105>.
- 590 Cummings, J. A., S. Smith, S. N. Carroll, and P. Spence, 2010: User’s Manual for the Navy
591 Coupled Ocean Data Assimilation 3D Variational Analysis (NCODA 3DVar) System, Version
592 3.0. URL <https://apps.dtic.mil/sti/html/trecms/AD1134364/index.html>.
- 593 D’Addezio, J. M., S. Smith, G. A. Jacobs, R. W. Helber, C. Rowley, I. Souopgui, and
594 M. J. Carrier, 2019: Quantifying wavelengths constrained by simulated SWOT obser-
595 vations in a submesoscale resolving ocean analysis/forecasting system. *Ocean Modelling*,
596 **135**, 40–55, <https://doi.org/10.1016/j.ocemod.2019.02.001>, URL [https://www.sciencedirect.
597 com/science/article/pii/S1463500318302166](https://www.sciencedirect.com/science/article/pii/S1463500318302166).
- 598 Daley, R., and E. Barker, 2001: NAVDAS: Formulation and Diagnostics. *Monthly Weather Re-
599 view*, **129** (4), 869–883, [https://doi.org/10.1175/1520-0493\(2001\)129<0869:NFAD>2.0.CO;2](https://doi.org/10.1175/1520-0493(2001)129<0869:NFAD>2.0.CO;2),
600 URL [https://journals.ametsoc.org/view/journals/mwre/129/4/1520-0493_2001_129_0869_nfad_
601 2.0.co_2.xml](https://journals.ametsoc.org/view/journals/mwre/129/4/1520-0493_2001_129_0869_nfad_2.0.co_2.xml).
- 602 Di Lorenzo, E., 2003: Seasonal dynamics of the surface circulation in the Southern California Cur-
603 rent System. *Deep Sea Research Part II: Topical Studies in Oceanography*, **50** (14), 2371–2388,
604 [https://doi.org/10.1016/S0967-0645\(03\)00125-5](https://doi.org/10.1016/S0967-0645(03)00125-5), URL [https://www.sciencedirect.com/science/
605 article/pii/S0967064503001255](https://www.sciencedirect.com/science/article/pii/S0967064503001255).

- 606 Egbert, G. D., and S. Y. Erofeeva, 2002: Efficient Inverse Modeling of Barotropic Ocean
607 Tides. *Journal of Atmospheric and Oceanic Technology*, **19** (2), 183–204, [https://doi.org/10.1175/1520-0426\(2002\)019<0183:EIMOBO>2.0.CO;2](https://doi.org/10.1175/1520-0426(2002)019<0183:EIMOBO>2.0.CO;2), URL https://journals.ametsoc.org/view/journals/atot/19/2/1520-0426_2002_019_0183_eimobo_2_0_co_2.xml.
609
- 610 Farrar, J. T., and Coauthors, 2025: S-MODE: The Sub-Mesoscale Ocean Dynamics
611 Experiment. *Bulletin of the American Meteorological Society*, **106** (4), E657–E677,
612 <https://doi.org/10.1175/BAMS-D-23-0178.1>, URL <https://journals.ametsoc.org/view/journals/bams/106/4/BAMS-D-23-0178.1.xml>.
613
- 614 Ferrari, R., and M. Nikurashin, 2010: Suppression of Eddy Diffusivity across Jets in the South-
615 ern Ocean. *Journal of Physical Oceanography*, **40** (7), 1501–1519, <https://doi.org/10.1175/2010JPO4278.1>, URL <https://journals.ametsoc.org/view/journals/phoc/40/7/2010jpo4278.1.xml>.
616
617
- 618 Ferrari, R., and C. Wunsch, 2009: Ocean Circulation Kinetic Energy: Reservoirs, Sources, and
619 Sinks. *Annual Review of Fluid Mechanics*, **41** (Volume 41, 2009), 253–282, <https://doi.org/10.1146/annurev.fluid.40.111406.102139>, URL <https://www.annualreviews.org/content/journals/10.1146/annurev.fluid.40.111406.102139>.
620
621
- 622 Fox-Kemper, B., R. Ferrari, and R. Hallberg, 2008: Parameterization of Mixed Layer Ed-
623 dies. Part I: Theory and Diagnosis. *Journal of Physical Oceanography*, **38** (6), 1145–1165,
624 <https://doi.org/10.1175/2007JPO3792.1>, URL <https://journals.ametsoc.org/view/journals/phoc/38/6/2007jpo3792.1.xml>.
625
- 626 Hogan, T. F., M. Liu, J. A. Ridout, M. S. Peng, and T. R. Whitcomb, 2015: The Navy Global
627 Environmental Model. *Oceanography*, **27** (3), 116–125, <https://doi.org/10.5670/oceanog.2014.73>, URL <https://tos.org/oceanography/article/the-navy-global-environmental-model>.
628
- 629 Holte, J., L. D. Talley, J. Gilson, and D. Roemmich, 2017: An Argo mixed layer climatol-
630 ogy and database. *Geophysical Research Letters*, **44** (11), 5618–5626, <https://doi.org/10.1002/2017GL073426>, URL <https://onlinelibrary.wiley.com/doi/abs/10.1002/2017GL073426>.
631
- 632 Khatri, H., S. M. Griffies, T. Uchida, H. Wang, and D. Menemenlis, 2021: Role of Mixed-Layer
633 Instabilities in the Seasonal Evolution of Eddy Kinetic Energy Spectra in a Global Subme-

634 soscale Permitting Simulation. *Geophysical Research Letters*, **48** (18), [https://doi.org/10.1029/](https://doi.org/10.1029/2021GL094777)
635 2021GL094777, URL <https://onlinelibrary.wiley.com/doi/abs/10.1029/2021GL094777>.

636 McGillicuddy, D. J., and Coauthors, 2007: Eddy/Wind Interactions Stimulate Extraordinary
637 Mid-Ocean Plankton Blooms. *Science*, **316** (5827), 1021–1026, [https://doi.org/10.1126/science.](https://doi.org/10.1126/science.1136256)
638 1136256, URL <https://www.science.org/doi/10.1126/science.1136256>.

639 Mellor, G. L., and T. Yamada, 1982: Development of a turbulence closure model for geo-
640 physical fluid problems. *Reviews of Geophysics*, **20** (4), 851–875, [https://doi.org/10.1029/](https://doi.org/10.1029/RG020i004p00851)
641 RG020i004p00851, URL <https://onlinelibrary.wiley.com/doi/abs/10.1029/RG020i004p00851>.

642 Metzger, E. J., O. M. Smedstad, P. G. Thoppil, H. E. Hurlburt, and J. A. Cummings, 2015:
643 US Navy Operational Global Ocean and Arctic Ice Prediction Systems. *Oceanography*,
644 **27** (3), 32–43, <https://doi.org/10.5670/oceanog.2014.66>, URL [https://tos.org/oceanography/](https://tos.org/oceanography/article/us-navy-operational-global-ocean-and-arctic-ice-prediction-systems)
645 [article/us-navy-operational-global-ocean-and-arctic-ice-prediction-systems](https://tos.org/oceanography/article/us-navy-operational-global-ocean-and-arctic-ice-prediction-systems).

646 Naveira-Garabato, A. C., X. Yu, J. Callies, R. Barkan, K. L. Polzin, E. E. Frajka-Williams,
647 C. E. Buckingham, and S. M. Griffies, 2022: Kinetic Energy Transfers between Mesoscale
648 and Submesoscale Motions in the Open Ocean’s Upper Layers. *Journal of Physical Oceanog-*
649 *raphy*, **52** (1), 75–97, <https://doi.org/10.1175/JPO-D-21-0099.1>, URL [https://journals.ametsoc.](https://journals.ametsoc.org/view/journals/phoc/52/1/JPO-D-21-0099.1.xml)
650 [org/view/journals/phoc/52/1/JPO-D-21-0099.1.xml](https://journals.ametsoc.org/view/journals/phoc/52/1/JPO-D-21-0099.1.xml).

651 Peng, Q., S.-P. Xie, D. Wang, R. X. Huang, G. Chen, Y. Shu, J.-R. Shi, and W. Liu,
652 2022: Surface warming–induced global acceleration of upper ocean currents. *Science Ad-*
653 *vances*, **8** (16), <https://doi.org/10.1126/sciadv.abj8394>, URL [https://www.science.org/doi/10.](https://www.science.org/doi/10.1126/sciadv.abj8394)
654 [1126/sciadv.abj8394](https://www.science.org/doi/10.1126/sciadv.abj8394).

655 Qiu, B., S. Chen, P. Klein, H. Sasaki, and Y. Sasai, 2014: Seasonal Mesoscale and Sub-
656 mesoscale Eddy Variability along the North Pacific Subtropical Countercurrent. *Journal of*
657 *Physical Oceanography*, **44** (12), 3079–3098, <https://doi.org/10.1175/JPO-D-14-0071.1>, URL
658 <https://journals.ametsoc.org/view/journals/phoc/44/12/jpo-d-14-0071.1.xml>.

659 Rai, S., M. Hecht, M. Maltrud, and H. Aluie, 2021: Scale of oceanic eddy killing by wind from
660 global satellite observations. *Science Advances*, **7** (28), <https://doi.org/10.1126/sciadv.abf4920>,
661 URL <https://www.science.org/doi/10.1126/sciadv.abf4920>.

- 662 Reichl, B. G., A. Adcroft, S. M. Griffies, and R. Hallberg, 2022: A Potential Energy Analysis of
663 Ocean Surface Mixed Layers. *Journal of Geophysical Research: Oceans*, **127** (7), [https://doi.org/](https://doi.org/10.1029/2021JC018140)
664 10.1029/2021JC018140, URL <https://onlinelibrary.wiley.com/doi/abs/10.1029/2021JC018140>.
- 665 Rocha, C. B., S. T. Gille, T. K. Chereskin, and D. Menemenlis, 2016: Seasonality of submesoscale
666 dynamics in the Kuroshio Extension. *Geophysical Research Letters*, **43** (21), 11,304–11,311,
667 <https://doi.org/10.1002/2016GL071349>, URL [https://onlinelibrary.wiley.com/doi/abs/10.1002/](https://onlinelibrary.wiley.com/doi/abs/10.1002/2016GL071349)
668 2016GL071349.
- 669 Sasaki, H., P. Klein, B. Qiu, and Y. Sasai, 2014: Impact of oceanic-scale interactions on the
670 seasonal modulation of ocean dynamics by the atmosphere. *Nature Communications*, **5** (1),
671 5636, <https://doi.org/10.1038/ncomms6636>, URL <https://doi.org/10.1038/ncomms6636>.
- 672 Schubert, R., J. Gula, R. J. Greatbatch, B. Baschek, and A. Biastoch, 2020: The
673 Submesoscale Kinetic Energy Cascade: Mesoscale Absorption of Submesoscale Mixed
674 Layer Eddies and Frontal Downscale Fluxes. *Journal of Physical Oceanography*, **50** (9),
675 2573–2589, <https://doi.org/10.1175/JPO-D-19-0311.1>, URL [https://journals.ametsoc.org/view/](https://journals.ametsoc.org/view/journals/phoc/50/9/jpoD190311.xml)
676 [journals/phoc/50/9/jpoD190311.xml](https://journals.ametsoc.org/view/journals/phoc/50/9/jpoD190311.xml).
- 677 Smagorinsky, J., 1963: GENERAL CIRCULATION EXPERIMENTS WITH THE PRIMITIVE
678 EQUATIONS: I. THE BASIC EXPERIMENT. *Monthly Weather Review*, **91** (3), 99–164,
679 [https://doi.org/10.1175/1520-0493\(1963\)091<0099:GCEWTP>2.3.CO;2](https://doi.org/10.1175/1520-0493(1963)091<0099:GCEWTP>2.3.CO;2), URL [https://journals.](https://journals.ametsoc.org/view/journals/mwre/91/3/1520-0493_1963_091_0099_gcewtp_2_3_co_2.xml)
680 [ametsoc.org/view/journals/mwre/91/3/1520-0493_1963_091_0099_gcewtp_2_3_co_2.xml](https://journals.ametsoc.org/view/journals/mwre/91/3/1520-0493_1963_091_0099_gcewtp_2_3_co_2.xml).
- 681 Tedesco, P. F., L. E. Baker, A. C. N. Garabato, M. R. Mazloff, S. T. Gille, C. P. Caulfield,
682 and A. Mashayek, 2023: Spatiotemporal Characteristics of the Near-Surface Turbulent Cas-
683 cade at the Submesoscale in the Drake Passage. *Journal of Physical Oceanography*, **54** (1),
684 187–215, <https://doi.org/10.1175/JPO-D-23-0108.1>, URL [https://journals.ametsoc.org/view/](https://journals.ametsoc.org/view/journals/phoc/54/1/JPO-D-23-0108.1.xml)
685 [journals/phoc/54/1/JPO-D-23-0108.1.xml](https://journals.ametsoc.org/view/journals/phoc/54/1/JPO-D-23-0108.1.xml).
- 686 Torres, H. S., P. Klein, D. Menemenlis, B. Qiu, Z. Su, J. Wang, S. Chen, and L.-L. Fu, 2018:
687 Partitioning Ocean Motions Into Balanced Motions and Internal Gravity Waves: A Modeling
688 Study in Anticipation of Future Space Missions. *Journal of Geophysical Research: Oceans*,
689 **123** (11), 8084–8105, <https://doi.org/10.1029/2018JC014438>, URL [https://onlinelibrary.wiley.](https://onlinelibrary.wiley.com/doi/abs/10.1029/2018JC014438)
690 [com/doi/abs/10.1029/2018JC014438](https://onlinelibrary.wiley.com/doi/abs/10.1029/2018JC014438).

- 691 Torres, H. S., and Coauthors, 2022: Separating Energetic Internal Gravity Waves and Small-Scale
692 Frontal Dynamics. *Geophysical Research Letters*, **49** (6), e2021GL096249, <https://doi.org/10.1029/2021GL096249>, URL <https://onlinelibrary.wiley.com/doi/abs/10.1029/2021GL096249>.
693
- 694 Torres, H. S., and Coauthors, 2024: Airborne observations of fast-evolving ocean sub-
695 mesoscale turbulence. *Communications Earth & Environment*, **5** (1), 771, <https://doi.org/10.1038/s43247-024-01917-3>, URL <https://www.nature.com/articles/s43247-024-01917-3>.
696
- 697 Vallis, G. K., 2017: *Atmospheric and Oceanic Fluid Dynamics: Fundamen-
698 tals and Large-Scale Circulation*. 2nd ed., Cambridge University Press, Cam-
699 bridge, <https://doi.org/10.1017/9781107588417>, URL [https://www.cambridge.org/core/books/
700 atmospheric-and-oceanic-fluid-dynamics/41379BDDC4257CBE11143C466F6428A4](https://www.cambridge.org/core/books/atmospheric-and-oceanic-fluid-dynamics/41379BDDC4257CBE11143C466F6428A4).
- 701 Zhang, Y., H. Xu, F. Qiao, and C. Dong, 2018: Seasonal variation of the global mixed layer
702 depth: comparison between Argo data and FIO-ESM. *Frontiers of Earth Science*, **12** (1), 24–36,
703 <https://doi.org/10.1007/s11707-017-0631-6>, URL <https://doi.org/10.1007/s11707-017-0631-6>.